

Contamination of polymethylmethacrylate by organic quantum emitters

Andre Neumann^{1,*}, Jessica Lindlau^{1,*}, and Alexander Högele¹

¹*Fakultät für Physik, Munich Quantum Center,
and Center for NanoScience (CeNS), Ludwig-Maximilians-Universität München,
Geschwister-Scholl-Platz 1, D-80539 München, Germany*

(Dated: June 27, 2017)

Abstract

We report the observation of ubiquitous contamination of polymethylmethacrylate by organic molecules with optical activity in the visible spectral range. Contamination sites of individual solvent-specific fluorophores in thin films of polymethylmethacrylate constitute fluorescence hot-spots with quantum emission statistics and quantum yields approaching 30% at cryogenic temperatures. Our findings not only resolve prevalent puzzles in the assignment of spectral features to various nanoemitters in polymer matrices, they also identify means for simple and cost-efficient realization of single-photon sources in the visible spectral range.

Embedding quantum emitters within chemically and electrostatically inert polymer matrices such as polymethylmethacrylate (PMMA) is a common approach to reduce the fluorescence (FL) intermittency encountered by a broad class of photoactive nanoparticles [1, 2] and molecular dyes [3] under ambient conditions, thus promoting stable and enhanced FL [4, 5]. However, contamination of the polymer matrix by fluorescent constituents can result in controversial assignment of spectral features. In some spectroscopy experiments it has proven difficult to distinguish between the FL stemming from quantum emitters, the polymer matrix, or the supporting substrate [6, 7]. This is not surprising given the challenge of unambiguous assignment of the FL to its actual source for photoactive systems with low quantum yields, or individual quantum emitters with high quantum yields but inherently low absolute FL intensities.

In the visible spectral range, the realm of photoactive nanoemitters includes single molecules [8], fluorescent nanodiamonds [9], colloidal quantum dots [10] and nanoplatelets [11], transition metal dichalcogenide quantum dots [12–15], or perovskite nanoplatelets [16]. The range of related potential applications in light emitting, detecting, and harvesting devices is as diverse as the specific details of the photophysics of the underlying emitters. In absolute terms, however, and depending on the radiative lifetime, some of these systems feature low FL intensities despite high quantum yields, while others suffer from reduced quantum yields due to optically inactive lowest-lying dark states [3, 17, 18] with strongly inhibited FL at cryogenic temperatures. Irrespective of the actual reason for low intensity, any contamination of the relevant FL by photoemissive substrates or matrices is clearly detrimental to both fundamental studies of nanoemitters and their related applications.

In the following, we present a comprehensive study targeting a quantitative analysis of the FL in the visible spectral range arising from a thin film of PMMA on various dielectric substrates. Surprisingly, we find that PMMA films prepared by standard solution-deposition procedures exhibit optical activity in the visible both at room and cryogenic temperatures. However, the FL is not a characteristic feature of the PMMA itself. It rather stems from fluorescent contaminants in the PMMA matrix that we ascribe to solvent residuals with specific FL intensity and spectra. For individual fluorescent contaminants, pronounced and spectrally stable zero-phonon lines (ZPLs) with red-shifted vibronic satellites and highly non-classical emission statistics emerge as a generic feature at cryogenic temperatures. At room temperature, thermal broadening of both the ZPL and the vibrational sidebands gives rise to a characteristic three-peak spectrum that can be mistaken for phonon replica of silica color centers [7] or subject to other interpretations [19–25].

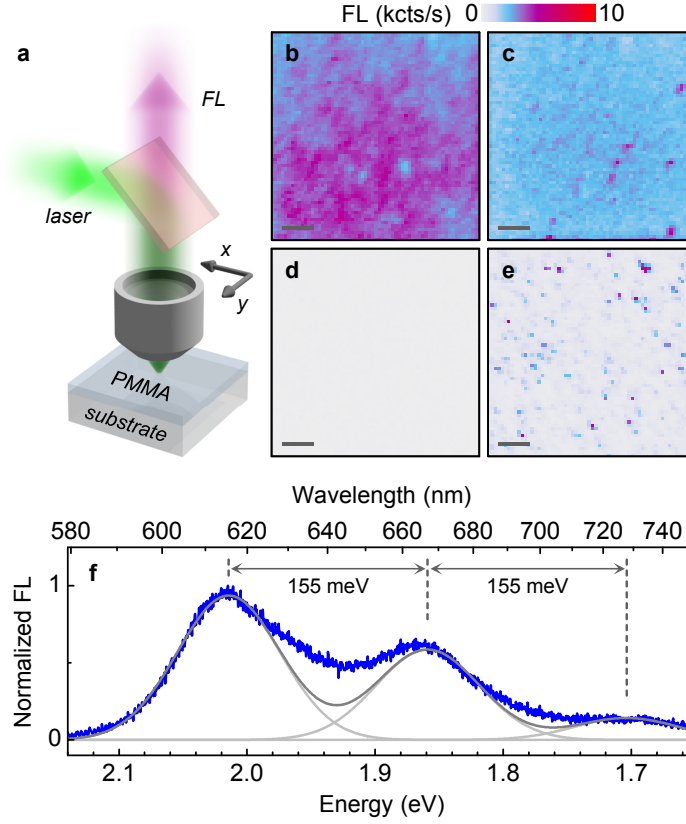


FIG. 1: **a**, Schematic of the experiment: fluorescence from dielectric substrates coated with a thin film of PMMA was studied with confocal raster-scan imaging and spectroscopy. Raster-scan fluorescence intensity maps of the surface of fused silica **b**, after sonication in acetone and isopropanol, **c**, additional sonication in deionized water, and **d**, oxygen plasma treatment. **e**, Fluorescence image of plasma-cleaned fused silica with a thin film of PMMA formulated in anisole. All maps were recorded with laser excitation at 532 nm and 130 kW/cm^2 ; the scale bars are $3 \mu\text{m}$. **f**, Fluorescence spectrum of a typical hotspot in PMMA with a fit by three Gaussian peaks with full-width at half-maximum linewidths of 90 meV and equidistant energy spacings of 155 meV.

The basics of our experiment are illustrated in Fig. 1a. We performed FL spectroscopy in a home-built optical microscope to study sample-specific emission in the spectral range of 560 – 770 nm excited with a continuous-wave laser at 532 nm, a wavelength frequently used to excite FL in the visible. By raster-scanning the sample with respect to fixed diffraction-limited confocal excitation and collection spots, we acquired maps of FL intensity as in Fig. 1b - e with a single photon counting avalanche photodiode (APD), and hyperspectral maps with spectrally dispersed FL as in

Fig. 1f recorded at each raster-scan pixel for spectral analysis of individual emission hotspots. The studies were complemented by time-correlated FL, second-order FL coherence and FL excitation spectroscopy experiments performed either at room temperature or at the cryogenic temperature of 3.1 K.

In the first stage of the experiments we studied the FL characteristics of bare dielectric substrates. It has been argued recently that silica-based substrates host intrinsic fluorescent centers with sizable FL intensity in the visible [7]. Therefore, we first investigated the FL from the surface of bare fused silica substrates exposed to different cleaning procedures (see Methods for details on cleaning protocols). Under ambient conditions and 250 μW irradiation in a full-width at half-maximum (FWHM) spot of 0.5 μm we acquired raster-scan FL maps shown in Fig. 1b - d. For fused silica sonicated subsequently in acetone and isopropanol according to a common cleaning procedure we observed FL from the entire sample surface with inhomogeneous intensity and an average APD count rate of ~ 4 kcts/s (Fig. 1b). After an additional sonication step in deionized water the level of FL decreased to an average of ~ 2 kcts/s away from hotspot emission with ~ 4 kcts/s (Fig. 1c). Most remarkably, additional treatment with oxygen plasma suppressed the FL from the silica surface below the dark count rate of the APD (Fig. 1d). This set of data, consistently observed for quartz and sapphire substrates subjected to oxygen plasma treatment (see the Supplementary Information for substrate-specific FL maps), clearly establishes the absence of intrinsic FL defects on silica substrates. Moreover, it provides a first hint at the source of the FL as stemming from organic surface contaminants that do not withstand oxygen plasma treatment.

For the second experimental stage we prepared substrates free of FL background and covered them by spin-coating with PMMA dissolved in anisole. On a silica substrate with 200 nm of PMMA, we observed the reappearance of fluorescent hotspots with intensities of up to ~ 6 kcts/s on a background of ~ 0.5 kcts/s (Fig. 1e) under measurement conditions identical to those of Fig. 1b - d. Similar results were found for as-deposited and thermally cross-linked PMMA films fabricated from anisole solutions (see Methods for sample details). For most hotspots, the FL was spatially localized to the diffraction-limited spot and characterized by room temperature spectra as in Fig. 1f. The spectrum with maximum FL at 2.02 eV (614 nm) can be reproduced with some success by three overlapping Gaussian peaks with FWHM linewidths of 90 meV, equidistant separations of 155 meV, and intensities that reduce with decreasing emission energy (grey solid lines in Fig. 1f). An explanation for the mismatch between this simplistic model fit and the actual spectrum pending, we point out its striking similarity to the spectra ascribed earlier to various

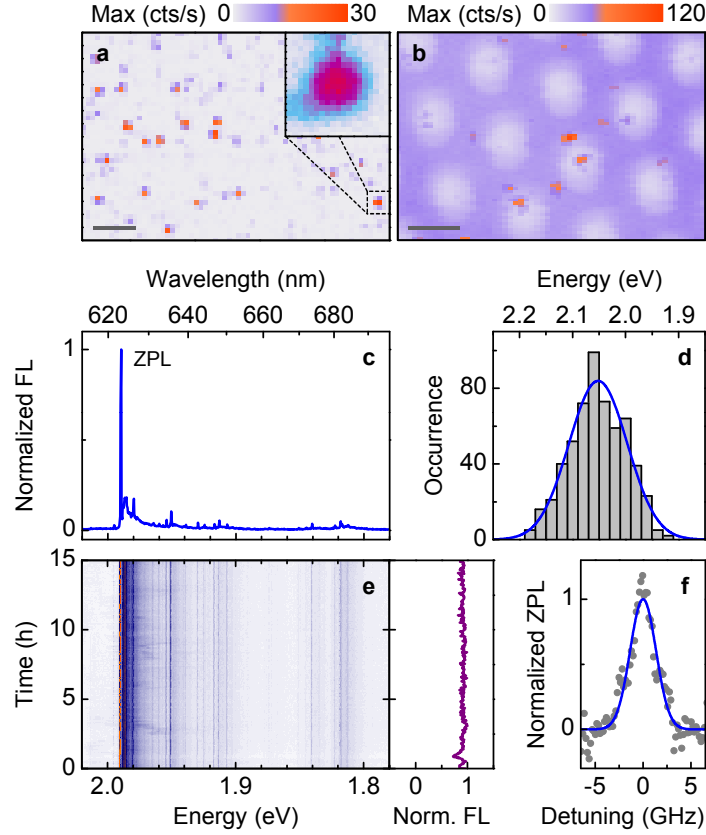


FIG. 2: **a** and **b**, Cryogenic fluorescence peak intensity maps of PMMA on a fused silica substrate and a perforated silicon nitride membrane, respectively (recorded with 532 nm laser excitation at 26 and 65 kW/cm²; the scale bars are 3 μ m). The inset in **a** shows a 5 \times zoom to the hotspot delimited by the dashed box. The grey circular areas in **b** are regions of freestanding PMMA. **c**, Normalized fluorescence spectrum of a typical hotspot with an intense zero-phonon line (ZPL) and redshifted satellites. **d**, Spectral distribution of the zero-phonon line of about 600 hotspots (the blue line is a Gaussian fit). **e**, Temporal evolution of the fluorescence spectrum (left) and normalized intensity (right) over 15 h for the hotspot with spectrum in **c**. **f**, Zero-phonon line spectrum resolved with a scanning Fabry-Pérot etalon (grey circles). The Gaussian fit (blue line) yields an inhomogeneous linewidth of 3.18 ± 0.13 GHz. All data were recorded at 3.1 K.

sources [6, 7, 19–23, 25]. Moreover, it exhibits a remarkable correspondence with the spectra of individual dyes in PMMA [26, 27], providing a second hint to hydrocarbon molecules as a source for misinterpretation and establishing a link to the visionary association made between the spectra of non-blinking colloidal quantum dots [23] and organic dyes [28].

To elucidate the correspondence between the FL hotspots found at room temperature in thin films

of PMMA and the spectral signatures of organic molecules we carried out spectroscopy studies at the cryogenic temperature of 3.1 K. Fig. 2a and b show representative cryogenic FL maps of PMMA films on a fused silica substrate and a perforated silicon nitride membrane, respectively. Both maps were acquired in the hyperspectral mode by recording spectrally dispersed FL with a nitrogen-cooled CCD and color-coding its maximum intensity at each raster-scan pixel. Note the conceptual difference to the raster-scan maps recorded with APDs: hyperspectral mapping emphasizes emitters with sharp FL peaks over spectrally broad FL background. Again, we found spatially localized emission from diffraction-limited hotspots (inset of Fig. 2a) analogous to our room temperature experiments. A few hotspots in Fig. 2b (with up to 120 cts/s) clearly stem from PMMA regions suspended over holes which can be unambiguously distinguished from the silicon nitride membrane by the respective FL background (grey and blue areas of the map correspond to intensities of 10 and 50 cts/s, respectively). This observation confirms once more that the PMMA film rather than the substrate is the actual host of FL hotspots.

A characteristic cryogenic FL spectrum of a hotspot in PMMA is shown in Fig. 2c. It features a narrow and intense peak, which we label as ZPL, accompanied by weak red-shifted satellites. More than 60% of localized emission sites exhibited similar spectral characteristics at low temperature. Within this group of emitters with spectrometer-limited ZPLs, 94% of hotspots constitute the class of emitters with a ZPL centered around 2.05 eV emission energy (605 nm emission wavelength). The corresponding normal distribution of the ZPL energy is shown in Fig. 2d, where the blue solid line is a Gaussian fit to the histogram with a FWHM of 130 meV. The remaining 6% of the single-site emitters with intense FL were characterized by two sharp ZPLs (see Supplementary Information for the corresponding normal distribution of emission energies) accompanied by red-shifted sidebands.

All spectra were remarkably stable over time without significant FL intermittence during the course of observation of 15 h (Fig. 2e) and beyond. Throughout the temporal evolution, the ZPL remained spectrometer-limited to one pixel of the CCD corresponding to an upper bound on the FWHM linewidth of 200 μ eV. A high-resolution spectrum recorded with a scanning Fabry-Pérot etalon suggests that spectral wandering broadens the ZPL on sub-minutes timescale to an inhomogeneous peak with a FWHM of 3.18 ± 0.13 GHz (Fig. 2f). These spectral signatures find their correspondence in the studies of hydrocarbon fluorophores embedded in a polymer host matrix [29–31]. Within this framework, low-temperature FL of single molecules is characterized by a spectrally narrow ZPL associated with the principal electronic transition [32] and sidebands stem-

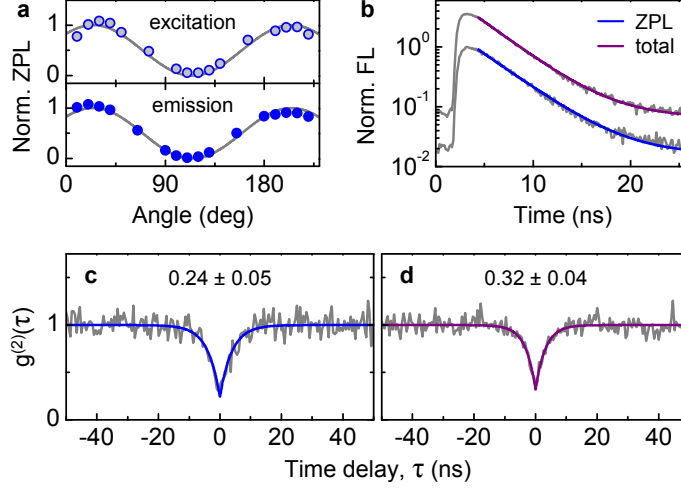


FIG. 3: **a**, Polarization characteristics of the zero-phonon line: normalized intensity as a function of the rotation angle of a linear polarizer in excitation and detection (top and bottom panels, respectively; the grey lines represent the same functional form of the fits to the data). **b**, Time-correlated decay of the zero-phonon line and the total fluorescence (grey traces) of a single hotspot, and corresponding monoexponential fits with decay constants of 3.8 and 3.6 ns (blue and purple traces). The plots were offset for clarity. **c** and **d**, Second-order coherence function $g^{(2)}(\tau)$ recorded with and without spectral selection of the zero-phonon line, respectively. The blue and purple lines are fits to the data with multi-photon probabilities of 0.24 ± 0.05 and 0.32 ± 0.04 . All data were recorded at 3.1 K with excitation at 532 nm.

ming from Franck-Condon transitions between vibronically dressed molecular electronic states [33, 34]. Stabilized in PMMA, single molecules exhibit FL with low intermittency and ZPLs limited by spectral diffusion to ~ 1 GHz [30, 35]. The red-shifted satellites of the ZPL are equally well pronounced in vibronic spectroscopy [36] of molecules with characteristic vibrational degrees of hydrocarbon complexes.

The set of data in Fig. 3 further substantiates the correspondence. With polarization-resolved measurements shown in Fig. 3a we confirmed the dipolar character associated with the molecular transition of the ZPL [27]. The orientation of the absorption and emission axes measured with linearly polarized excitation and detection, respectively, were determined as collinear within our experimental precision. Furthermore, time-correlated measurements of Fig. 3b revealed the characteristic FL decay dynamics of molecules on nanoseconds timescale [37]. The single-exponential lifetimes of 3.8 and 3.6 ns for the ZPL within a spectral window of 60 meV and the total FL in-

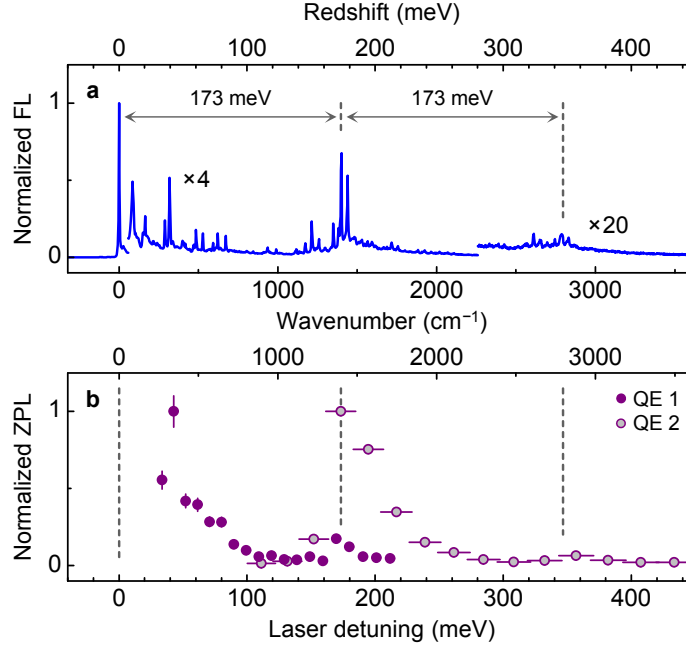


FIG. 4: **a**, Normalized fluorescence spectrum of a typical hotspot recorded with excitation at 532 nm and plotted as a function of spectral redshift from the zero-phonon line at 2.134 eV. The intensity was magnified by a factor of 4 (20) above 7 meV (280 meV) redshift to highlight two groups of phonon sidebands with a spacing of 173 meV. **b**, Normalized zero-phonon line intensity as a function of excitation laser detuning for two quantum emitters (QE) with spectral features as in **a** recorded within excitation wavelength intervals of 538 – 583 and 485 – 555 nm (solid and open circles, respectively). All data were recorded at 3.1 K.

tensity, respectively, were the same within the temporal resolution of ~ 0.3 ns in our experiments, identifying red-shifted sidebands as vibronic ZPL replicas. Finally, single photon emission statistics as a hallmark of single-molecule FL [38, 39] are presented in Fig. 3c and d. With photon correlation spectroscopy we observed pronounced photon antibunching in the normalized second-order coherence function $g^{(2)}(\tau)$ at zero time delay for both the FL within a band-pass interval of 60 meV around the ZPL (with $g^{(2)}(0) = 0.24 \pm 0.05$ in Fig. 3c) and the full FL spectrum without spectral filtering ($g^{(2)}(0) = 0.32 \pm 0.04$ in Fig. 3d). Thus, within the uncertainty of our measurement, we can rule out simultaneous photon emission into the ZPL and the sideband spectrum associated with the vibronic ZPL satellites.

Having identified the fluorescent hotspots in PMMA as single fluorescent molecules, we utilized vibrationally resolved FL spectroscopy [34, 36, 40] to shed light on their molecular nature. Fig. 4a

shows a spectrum of a hotspot that is representative for fluorescent contaminants in PMMA prepared with anisole as solvent. A series of low-frequency vibrational modes contributes to the sidebands below 80 meV (645 cm^{-1}), followed by a group of replicas around 173 meV (1395 cm^{-1}) and a weaker satellite group around 346 meV (2790 cm^{-1}). The latter is in fact a second harmonic of the preceding group as confirmed by correlation analysis between all individual peaks of the two groups upon a spectral shift by 173 meV. All main vibrational features in emission have their broadened counterpart resonances in absorption, as demonstrated by the FL excitation spectra in Fig. 4b recorded for two typical emitters with different ZPL energies as a function of laser energy detuning at constant excitation power. For both quantum emitters of Fig. 4b, the absorption is enhanced whenever the laser detuning with respect to the ZPL matches the energy of the vibronic sidebands (the dashed lines in Fig. 4 emphasize the correspondence between the resonances in emission and absorption).

The vibrationally resolved spectrum of Fig. 4b is typical for fluorescent molecules in PMMA films from anisole-based solutions. It exhibits a striking similarity with the cryogenic FL of anthracene characterized by a ZPL in the ultraviolet (around 3 eV) and a pronounced vibronic satellite group around 1400 cm^{-1} redshifts [41]. The according vibrational degrees of freedom are related to the intramolecular stretching of adjacent carbon bonds in polycyclic aromatic hydrocarbons [34]. The observation of the ZPL emission in the visible (around 2 eV) from anisole-based PMMA suggests that the optical activity of solvent-related contaminants in such films stems from acene chains such as pentacene, or from anthracene-derived dyes such as alizarin.

We applied vibrational FL spectroscopy to hotspots in PMMA films derived from other solvents (see Methods for sample preparation details). As highlighted by the raster-scan maps of Fig. 5, the areal density and the FL intensity of hotspots in PMMA films formed with chlorobenzene (Fig. 5a, b), methyl isobutyl ketone (Fig. 5c, d) and toluene (Fig. 5g, h) were similar to anisole-based PMMA characteristics (Fig. 1e and Fig. 2a). The vibronic signatures, however, showed significant differences. Fig. 5c, f, and i show normalized average spectra of 25 brightest fluorophore contaminants in PMMA films prepared with different solvents (see the Supplementary Information for the corresponding average spectrum of anisole-based PMMA).

The spectrum of a typical hotspot in chlorobenzene-based PMMA features a low-frequency vibronic band around 250 cm^{-1} and a pronounced high-frequency band around 1400 cm^{-1} discussed earlier (as indicated by the diamond and the hexagon Fig. 5c). In contrast, the vibronic FL characteristics of hotspots in PMMA films formed with methyl isobutyl ketone and toluene solu-

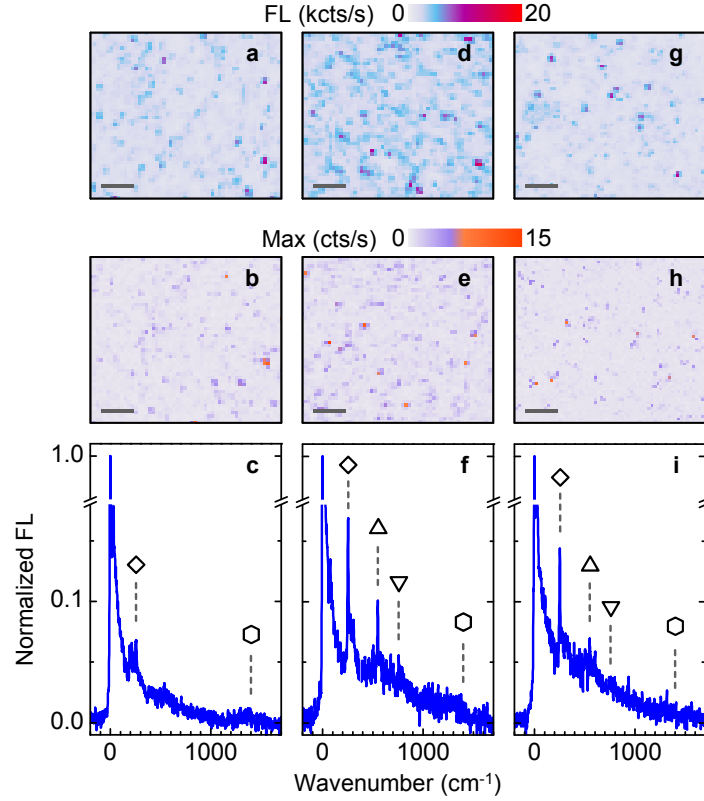


FIG. 5: **a, b**, Raster-scan maps of integrated fluorescence intensity and spectrally dispersed fluorescence maxima, respectively, for PMMA dissolved with chlorobenzene. **d, e**, and **g, h**, Same for PMMA films prepared by solution in methyl isobutyl ketone and toluene, respectively. All scale bars are 3 μm . **c, f**, and **i** Average fluorescence spectra of 25 most intense hotspots in PMMA dissolved in chlorobenzene, methyl isobutyl ketone, and toluene, respectively, displayed as a function of the redshift from the zero-phonon line. The symbols indicate specific vibronic modes of hydrocarbon-based molecular dyes. All data were recorded at 3.1 K with laser excitation at 532 nm and 52 kW/cm² on thermally annealed PMMA films of 200 nm thickness on oxygen plasma-cleaned fused silica.

tions (Fig. 5f and i, respectively) exhibit additional vibrational signatures at 548 and 757 cm⁻¹. The vibronic modes, labelled with diamonds and upper and lower triangles in Fig. 5c, f, and i are characteristic of rylene dyes composed of naphthalenes. While the low-frequency mode (diamonds in Fig. 5c, f, and i) is close to that of the long axis stretch of a terrylene molecule, the higher-frequency modes (upper and lower triangles in Fig. 5f and i) are consistent with the short axis stretch and ring deformation of outer naphthalenes, respectively [34]. Note that naphthalene-related bands of rylene dyes are only very weakly expressed in the averaged vibronic FL spectra

observed in anisole- and chlorobenzene-based PMMA films (Fig. 4a and Fig. 5c).

In addition to solvent-specific differences in the spectra of fluorescent hotspots in PMMA, vibrationally resolved FL spectroscopy identifies the normal modes of aromatic hydrocarbons around 170 meV (1400 cm^{-1}) as a generic feature of FL contaminants at low temperatures. At elevated temperatures, these modes develop into broad vibronic satellites (see the Supplementary Information for FL spectra at different temperatures) that accompany the FL from the thermally broadened principal molecular transition. With this in mind, the interpretation of the three-peak structure of the room-temperature FL spectrum in Fig. 1f as arising from an organic fluorophore is straight forward. For an adequate modelling, however, the contributions of all other vibrational modes must be taken into account. The main corrections to the inhomogeneous spectral profile of the ZPL and the vibronic modes of polycyclic hydrocarbons will naturally appear on the low-energy side of the peaks, where the fit with three Gaussians most significantly deviates from the actual spectrum.

In concise terms, our comprehensive study of fluorescent spots, ubiquitously present in PMMA films and on contaminated dielectric substrates, leads to the conclusion that organic fluorophores are the actual source of misinterpreted FL signatures. We estimate the quantum yield of such organic quantum emitters to range from $\sim 5\%$ at room temperature up to 30% at 3.1 K (see the Supplementary Information for the estimate of the quantum yield). These values are not remarkably high, however, the corresponding FL intensity can be significant in studies of photoactive systems with reduced quantum yields in cryogenic or ambient environments. In fact, we found the FL intensity of PMMA hotspots to be roughly a third of the emission intensity of individual terrylenediimide (TDI) molecules at cryogenic temperatures, and in many instances even more intense than commercial radiant dyes at ambient conditions. Given the present technological limitations to solvent purity, it seems unlikely that contamination of PMMA and other polymer matrices can be completely avoided in future experiments. On the other hand, the abundance of stable quantum emitters in polymer films could facilitate a range of fundamental studies and technological developments relying on simple and cheap sources of non-classical light.

Methods: All samples were prepared in a clean-room environment. Unless stated otherwise, substrates were cleaned by initial sonication in acetone (Technic, acetone Micropur VLSI) for 5 min, followed by isopropanol (Technic, propan-2-ol Micropur VLSI) for 5 min, and finally exposed for 1 min to oxygen plasma. Polymer covered samples were prepared by spin-coating $\sim 10\text{ }\mu\text{l}$ of PMMA onto oxygen plasma-treated fused silica (CrysTec) and other dielectric substrates (quartz and sapphire). An ellipsometer was used to adjust the spin-coating parameters for a film thick-

ness of 200 nm. The films were obtained from commercial PMMA formulated in anisole with a molecular weight of 950K (MicroChem, 950PMMA A4 resist for electron-beam lithography). The spin-coated PMMA film was left to dry at ambient conditions. Optionally, the samples were baked at 180 °C for 90 s on a hot plate. The perforated silicon nitride membrane (PELCO) of Fig. 2b was drop-casted and baked to ensure mechanical stability of freely suspended PMMA. Control experiments were carried out with 4% of 450K PMMA resin (DuPont, Elvacite 2041) diluted in 96% of chlorobenzene (Merck, 801791), methyl isobutyl ketone (Technic, MIBK Micropur VLSI), or toluene (Sigma-Aldrich, 179418).

FL imaging and spectroscopy measurements were performed with a home-built confocal microscope coupled to single-mode fibers. Room-temperature experiments were conducted with an apochromatic objective with numerical aperture (NA) of 0.82 (attocube systems, LT-APO/VISIR/0.82) and an oil immersion objective (Olympus, UPLFLN 100XOI2) with NA of 1.30 for the data in Fig. 1f. Cryogenic experiments were carried out in a helium bath cryostat or a low-vibration closed-cycle cryostat (attocube systems, attoDRY1000) with base temperatures of 4.2 K and 3.1 K, respectively, using a low-temperature apochromatic objective with NA of 0.65 (attocube systems, LT-APO/VIS/0.65).

Continuous wave excitation with a solid-state laser at 532 nm (CNI, MLL-III-532-50-1) was used in all experiments except for the measurements of data in Fig. 3b and Fig. 4b. All FL maps were recorded with circularly polarized excitation except for Fig. 2b and Fig. S1, where linearly polarized excitation was used. Time-resolved FL data in Fig. 3b were measured with ps-excitation at 532 nm. The FL excitation experiments of Fig. 4b were performed with an optical parametric oscillator (Coherent, Mira-OPO with a FWHM spectral bandwidth of 0.5 nm) or a spectrally filtered supercontinuum laser (NKT Photonics, SuperK EXW-12 with a FWHM spectral bandwidth of 5.5 nm). Single photon counting avalanche photodiodes (PicoQuant, τ -SPADs with dark count rates of 35 cts/s and a temporal resolution of 320 ps) or a monochromator equipped with a liquid nitrogen cooled CCD (PI, Acton SP-2558 and Spec-10:100BR/LN with a spectral resolution of 200 μ eV and a gain setting of 4 e⁻/count) were used for detection. The hyperspectral raster-scan maps in Fig. 2a and b were recorded in the spectral range of 1.68–2.20 eV. The data in Fig. 2f were measured with a home-built monolithic scanning Fabry-Pérot etalon with a spectral resolution of 150 MHz and a scanning rate of 5.5 MHz/s.

Conflict of interest: The authors declare no competing financial interest.

Acknowledgment. We thank T. Basché, C. Bräuchle, I. Gerhard, S. Götzinger, K. Karrai, J. P. Kot-

thaus, E. Lifshitz, J. Lupton, G. I. Maikov, M. Pilo-Pais, I. Pugliesi, K. Puschkarsky, E. Riedle, J. Tilchin and S. E. Beavan for helpful discussions and useful input at various stages of the project, P. Maletinsky and S. Thoms for providing samples with NV centers in diamond and TDI molecules in PMMA, respectively, and P. Altpeter and R. Rath for assistance in the clean-room. This work was funded by the Volkswagen Foundation, the German-Israeli Foundation for Scientific Research and Development (GIF), and the Deutsche Forschungsgemeinschaft (DFG) Cluster of Excellence Nanosystems Initiative Munich (NIM) with financial support from LMUinnovativ and the Center for NanoScience (CeNS). A. H. acknowledges funding by the European Research Council under the ERC grant agreement no. 336749.

Author Contributions: *these authors contributed equally to this work.

Corresponding author: alexander.hoegele@lmu.de

Supplementary Information provides details on sample fabrication and experiments.

-
- [1] M. Nirmal, B. O. Dabbousi, M. G. Bawendi, J. J. Macklin, J. K. Trautman, T. D. Harris, and L. E. Brus, *Nature* **383**, 802 (1996).
 - [2] P. Frantsuzov, M. Kuno, B. Janko, and R. A. Marcus, *Nat. Phys.* **4**, 519 (2008).
 - [3] T. Basché, S. Kummer, and C. Bräuchle, *Nature* **373**, 132 (1995).
 - [4] C. Bradac, T. Gaebel, N. Naidoo, M. J. Sellars, J. Twamley, L. J. Brown, A. S. Barnard, T. Plakhotnik, A. V. Zvyagin, and J. R. Rabeau, *Nat. Nanotechnol.* **5**, 345 (2010).
 - [5] N. Ai, W. Walden-Newman, Q. Song, S. Kalliakos, and S. Strauf, *ACS Nano* **5**, 2664 (2011).
 - [6] X. Wang, X. Ren, K. Kahen, M. A. Hahn, M. Rajeswaran, S. Maccagnano-Zacher, J. Silcox, G. E. Cragg, A. L. Efros, and T. D. Krauss, *Nature* **527**, 544 (2015).
 - [7] F. T. Rabouw, N. M. B. Cogan, A. C. Berends, W. v. d. Stam, D. Vanmaekelbergh, A. F. Koenderink, T. D. Krauss, and C. d. M. Donega, *Sci. Rep.* **6**, 21187 (2016).
 - [8] T. Basché, W. E. Moerner, M. Orrit, and U. P. Wild, eds., *Single-Molecule Optical Detection, Imaging and Spectroscopy* (VCH Verlagsgesellschaft mbH, 1997).
 - [9] I. Aharonovich, A. D. Greentree, and S. Praver, *Nat. Photonics* **5**, 397 (2011).
 - [10] V. I. Klimov, S. A. Ivanov, J. Nanda, M. Achermann, I. Bezel, J. A. McGuire, and A. Piryatinski, *Nature* **447**, 441 (2007).
 - [11] S. Ithurria, M. D. Tessier, B. Mahler, R. P. S. M. Lobo, B. Dubertret, and A. L. Efros, *Nat. Mater.* **10**,

- 936 (2011).
- [12] A. Srivastava, M. Sidler, A. V. Allain, D. S. Lembke, A. Kis, and A. Imamoğlu, *Nat. Nanotechnol.* **10**, 491 (2015).
 - [13] Y.-M. He, G. Clark, J. R. Schaibley, Y. He, M.-C. Chen, Y.-J. Wei, X. Ding, Q. Zhang, W. Yao, X. Xu, et al., *Nat. Nanotechnol.* **10**, 497 (2015).
 - [14] M. Koperski, K. Nogajewski, A. Arora, V. Cherkez, P. Mallet, J.-Y. Veuillen, J. Marcus, P. Kossacki, and M. Potemski, *Nat. Nanotechnol.* **10**, 503 (2015).
 - [15] C. Chakraborty, L. Kinnischtzke, K. M. Goodfellow, R. Beams, and A. N. Vamivakas, *Nat. Nanotechnol.* **10**, 507 (2015).
 - [16] M. C. Weidman, M. Seitz, S. D. Stranks, and W. A. Tisdale, *ACS Nano* **10**, 7830 (2016).
 - [17] A. L. Efros, M. Rosen, M. Kuno, M. Nirmal, D. J. Norris, and M. Bawendi, *Phys. Rev. B* **54**, 4843 (1996).
 - [18] X.-X. Zhang, Y. You, S. Y. F. Zhao, and T. F. Heinz, *Phys. Rev. Lett.* **115**, 257403 (2015).
 - [19] M. D. Mason, G. M. Credo, K. D. Weston, and S. K. Buratto, *Phys. Rev. Lett.* **80**, 5405 (1998).
 - [20] D. S. English, L. E. Pell, Z. Yu, P. F. Barbara, and B. A. Korgel, *Nano Lett.* **2**, 681 (2002).
 - [21] J. Martin, F. Cichos, F. Huisken, and C. von Borczyskowski, *Nano Lett.* **8**, 656 (2008).
 - [22] A. M. Chizhik, A. I. Chizhik, R. Gutbrod, A. J. Meixner, T. Schmidt, J. Sommerfeld, and F. Huisken, *Nano Lett.* **9**, 3239 (2009).
 - [23] X. Wang, X. Ren, K. Kahen, M. A. Hahn, M. Rajeswaran, S. Maccagnano-Zacher, J. Silcox, G. E. Cragg, A. L. Efros, and T. D. Krauss, *Nature* **459**, 686 (2009).
 - [24] K. Kůsová, O. Cibulka, K. Dohnalová, I. Pelant, J. Valenta, A. Fučíková, K. Žídek, J. Lang, J. Englich, P. Matějka, et al., *ACS Nano* **4**, 4495 (2010).
 - [25] T. Schmidt, A. I. Chizhik, A. M. Chizhik, K. Potrick, A. J. Meixner, and F. Huisken, *Phys. Rev. B* **86**, 125302 (2012).
 - [26] J. K. Trautman, J. J. Macklin, L. E. Brus, and E. Betzig, *Nature* **369**, 40 (1994).
 - [27] J. J. Macklin, J. K. Trautman, T. D. Harris, and L. E. Brus, *Science* **272**, 255 (1996).
 - [28] M. Orrit and T. Basché, *Chem. Phys. Chem.* **10**, 2383 (2009).
 - [29] R. Kettner, J. Tittel, T. Basché, and C. Bräuchle, *J. Phys. Chem.* **98**, 6671 (1994).
 - [30] B. Kozankiewicz, J. Bernard, and M. Orrit, *J. Chem. Phys.* **101**, 9377 (1994).
 - [31] A. Walser, A. Renn, S. Götzinger, and V. Sandoghdar, *Chem. Phys. Lett.* **472**, 44 (2009).
 - [32] F. P. Diehl, C. Roos, H.-C. Jankowiak, R. Berger, A. Köhn, G. Diezemann, and T. Basché, *J. Phys.*

Chem. B **114**, 1638 (2010).

- [33] P. Tchénio, A. B. Myers, and W. Moerner, Chem. Phys. Lett. **213**, 325 (1993).
- [34] A. B. Myers, P. Tchénio, M. Z. Zgierski, and W. E. Moerner, J. Phys. Chem. **98**, 10377 (1994).
- [35] A. Walser, G. Zumofen, A. Renn, S. Götzinger, and V. Sandoghdar, Mol. Phys. **107**, 1897 (2009).
- [36] P. Tchénio, A. B. Myers, and W. E. Moerner, J. Phys. Chem. **97**, 2491 (1993).
- [37] A. P. Green and A. R. Buckley, Phys. Chem. Chem. Phys. **17**, 1435 (2015).
- [38] T. Basché, W. E. Moerner, M. Orrit, and H. Talon, Phys. Rev. Lett. **69**, 1516 (1992).
- [39] B. Lounis and W. E. Moerner, Nature **407**, 491 (2000).
- [40] W. E. Moerner and L. Kador, Phys. Rev. Lett. **62**, 2535 (1989).
- [41] W. Helfrich and F. R. Lipsett, J. Chem. Phys. **43**, 4368 (1965).

SUPPLEMENTARY INFORMATION

Sample fabrication

All samples were prepared in a clean-room environment. Unless stated otherwise, substrates were cleaned by initial sonication in acetone (Technic, acetone Micropur VLSI) for 5 min, followed by isopropanol (Technic, propan-2-ol Micropur VLSI) for 5 min, and finally exposed for 1 min to oxygen plasma. Polymer covered samples were prepared by spin-coating $\sim 10 \mu\text{l}$ of PMMA onto oxygen plasma-treated fused silica (CrysTec) and other dielectric substrates (quartz and sapphire). An ellipsometer was used to adjust the spin-coating parameters for a film thickness of 200 nm. The films were obtained from commercial anisole based PMMA with a molecular weight of 950K (MicroChem, 950PMMA A4 resist for electron-beam lithography). The spin-coated PMMA film was left to dry at ambient conditions. Optionally, the samples were baked at 180 °C for 90 s on a hot plate. The perforated silicon nitride membrane (PELCO) of Fig. 1b from the main text was drop-casted and baked to ensure mechanical stability of freely suspended PMMA. Control experiments were carried out with 4% of 450K PMMA resin (DuPont, Elvacite 2041) diluted in 96% of chlorobenzene (Merck, 801791), methyl isobutyl ketone (Technic, MIBK Micropur VLSI), or toluene (Sigma-Aldrich, 179418).

Experimental setup

A home-built confocal microscope coupled to single-mode fibers was used for FL imaging and spectroscopy. Room-temperature experiments were performed with an apochromatic objective with numerical aperture (NA) of 0.82 (attocube systems, LT-APO/VISIR/0.82) and an oil immersion objective (Olympus, UPLFLN 100XOI2) with NA of 1.30. Cryogenic experiments were carried out in a helium dewar or a low-vibration closed-cycle cryostat (attocube systems, at-toDRY1000) with base temperatures of 4.2 K and 3.1 K, respectively, using a low-temperature apochromatic objective with NA of 0.65 (attocube systems, LT-APO/VIS/0.65). The FL was excited with a continuous wave solid-state laser at 532 nm (CNI, MLL-III-532-50-1), an optical parametric oscillator (Coherent, Mira-OPO with a FWHM spectral bandwidth of 0.5 nm), or a spectrally filtered supercontinuum laser (NKT Photonics, SuperK EXW-12 with a FWHM spectral bandwidth of 5.5 nm). Single photon counting avalanche photodiodes (PicoQuant, τ -SPADs with dark count rates of 35 cts/s and a temporal resolution of 320 ps) or a monochromator equipped with

a liquid nitrogen cooled CCD (PI, Acton SP-2558 and Spec-10:100BR/LN with a spectral resolution of $200 \mu\text{eV}$ and a gain setting of $4 \text{e}^-/\text{count}$) were used for detection. A home-built monolithic scanning Fabry-Pérot etalon with a spectral resolution of 150 MHz was used for high-resolution spectroscopy.

Optical characterization of substrates

Three dielectric substrates were studied in hyperspectral raster-scan FL: fused silica (Crystec), quartz (Crystec, z-cut, 0001 orientation) and sapphire (MaTecK, z-cut, 0001 orientation). Prior to cryogenic measurements the substrates were exposed to oxygen plasma. Cryogenic raster-maps of FL maxima are shown in Fig. 1a, b, and c for fused silica, quartz, and sapphire, respectively. The FL maximum level was identical for fused silica and quartz (Fig. 1a and b) with count rates given by the readout noise of the liquid nitrogen cooled CCD. The sapphire substrate exhibited spatially homogeneous FL intensity stemming from a sharp peak at $\sim 694 \text{ nm}$ (1.787 eV) of the R-line of Cr^{3+} ions in Al_2O_3 .

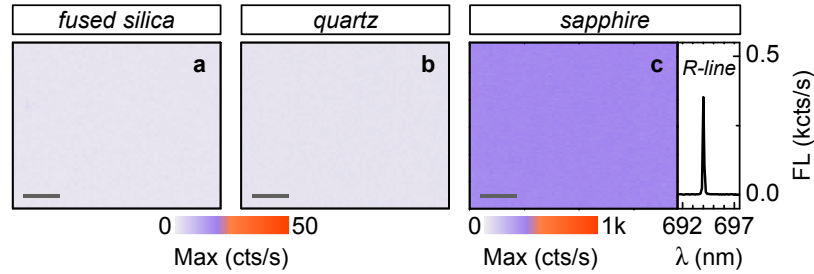


FIG. 1: **a**, **b**, and **c**, Raster-scan maps of spectrally dispersed fluorescence maxima for oxygen plasma-treated fused silica, quartz, and sapphire substrate, respectively. The hyperspectral maps were recorded between 1.68 eV and 2.20 eV with a binning of 0.4 meV at an excitation power density of $130 \text{ kW}/\text{cm}^2$. The temperature was 3.1 K. The fluorescence intensity levels in **a** and **b** correspond to the readout noise of the CCD, the homogeneous level of 1 kcts/s in **c** corresponds to the R-line emission at $\sim 694 \text{ nm}$ (1.787 eV) of Cr^{3+} ions in sapphire with a characteristic spectrum shown in the right panel. All data were measured with a linearly polarized 532 nm laser; scale bars are $3 \mu\text{m}$.

Optical characterization of PMMA prepared with different solvents

Fig. 2 compares cryogenic FL characteristics of PMMA films with 200 nm thickness, prepared by spin-coating mixtures of PMMA in different solvents onto oxygen plasma-treated fused silica

substrates. Four different solvents were used: anisole (sample A), chlorobenzene (sample C), methyl isobutyl ketone (sample M), and toluene (sample T).

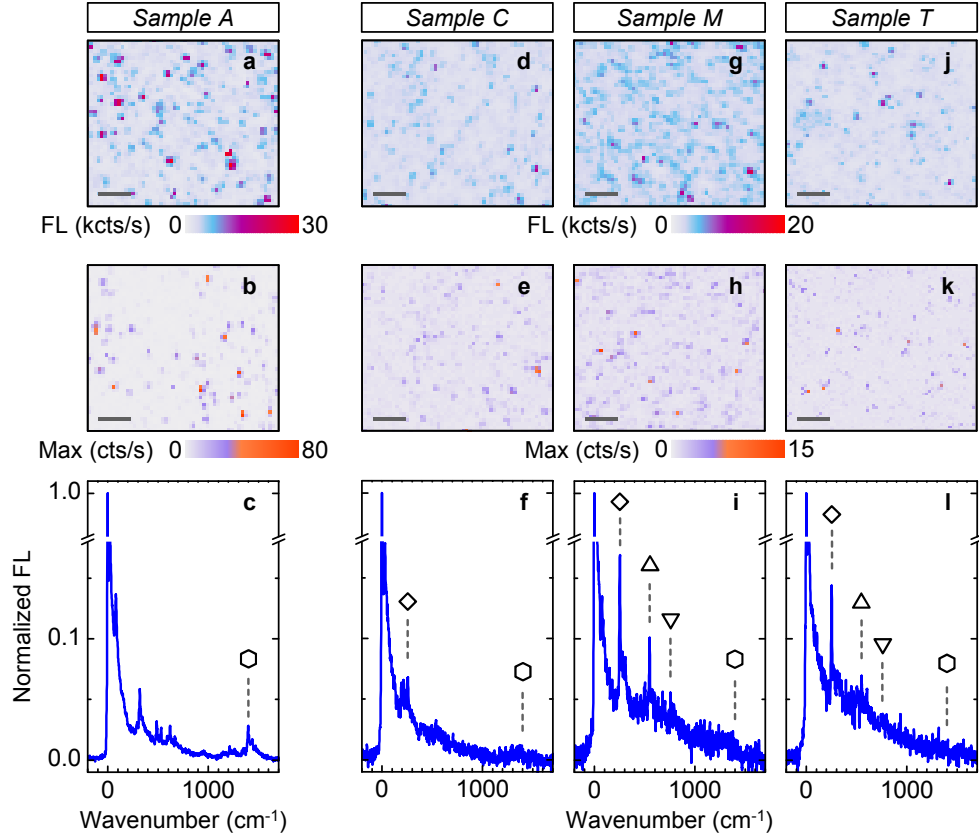


FIG. 2: **a**, and **b**, Raster-scan maps of integrated fluorescence intensity and spectrally dispersed fluorescence maxima, respectively, for PMMA dissolved with anisole. **d** and **e**, **g** and **h**, **j** and **k**, Same for PMMA films prepared with chlorobenzene, methyl isobutyl ketone, and toluene solutions, respectively. **c**, Normalized ensemble spectrum of 25 brightest fluorescence hotspots in anisole-based PMMA, plotted in wavenumbers as a function of red-shift from the zero-phonon line. **f**, **i**, and **l**, Same for PMMA formed with chlorobenzene, methyl isobutyl ketone, and toluene, respectively. Symbols indicate to hydrocarbon-specific vibronic modes of molecular dyes (see main text). All data were measured on thermally annealed PMMA films of 200 nm thickness on oxygen plasma-cleaned fused silica substrates at 3.1 K. The samples were excited at 532 nm with a power density of 52 kW/cm² and circular polarization. All scale bars are 3 μ m. The data in **d** - **l** are the same as in Fig. 5 of the main text.

Spectral characteristics of quantum emitters in anisole-based PMMA films

Representative spectra of most common hotspot quantum emitters in PMMA films prepared with anisole solvent are shown in Fig. 3. More than 60% of localized emission sites exhibited similar spectral characteristics at low temperature. Within this group of emitters with spectrometer-limited ZPLs, 94% of hotspots constituted the class of emitters with one sharp and intense zero-phonon line (ZPL) and red-shifted vibronic replicas as in Fig. 3a. The corresponding normal distribution of the ZPL energy is shown in Fig. 3b. In contrast to such emitters that we label here as type 1, 6% of type 2 fluorescent hotspots exhibited two intense and sharp peaks as in Fig. 3c with two intense vibronic satellites and a much narrower spread in the energy of the blue-most peak (histogram in Fig. 3d).

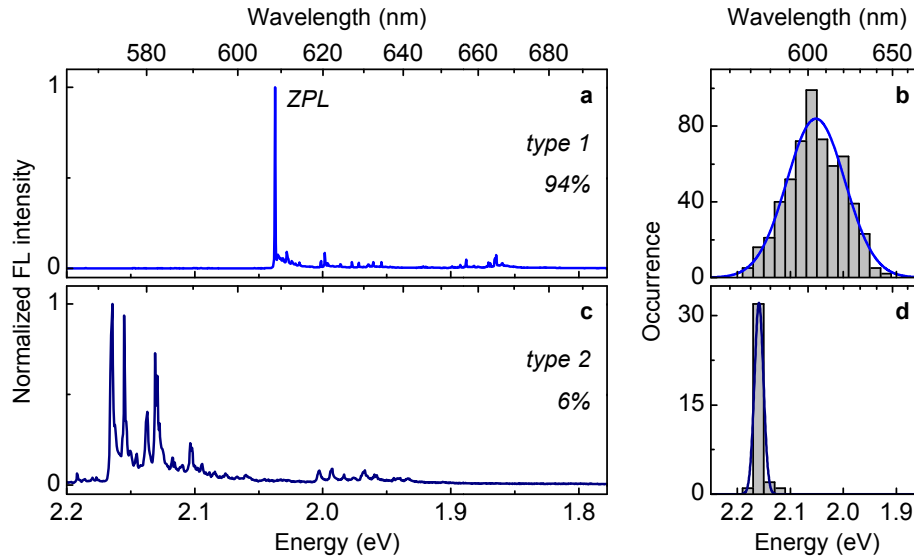


FIG. 3: **a**, Normalized fluorescence spectrum of a hotspot with an intense zero-phonon line (ZPL) and red-shifted satellites typical for type 1 quantum emitters in anisole-based PMMA. **b**, Spectral distribution of the zero-phonon line of about 600 such hotspots (same as in Fig. 2d in the main text). **c**, Representative normalized spectrum of type 2 hotspot emitters featuring two intense and sharp emission peaks with two intense vibronic satellites. **d**, Corresponding energy distribution of the blue-most peak in type 2 emission spectrum. The fraction of type 1 and emitters 2 is given in percent in **a** and **c**, respectively. The blue lines in **b** and **d** are normal distribution fits with full-widths at half-maximum of 130 and 20 meV, respectively. All data were measured at 3.1 K and excitation at 532 nm.

The evolution of a typical type 1 hotspot spectrum with temperature in sample A (anisole-based PMMA) is shown in Fig. 4. The ZPL and the vibronic satellites broadened upon heating from 4 to 41 K (Fig. 4b), and the overall FL decreased gradually for temperatures above ~ 25 K (Fig. 4c).

Both the initial intensity and the spectral lineshape were recovered upon successive cooling back to 4 K. The trend of thermal broadening as in Fig. 4b eventually results in significant spectral overlap of the ZPL and vibronic satellites at room temperature with predominant contributions from the vibronic group around ~ 155 meV and its second harmonic around ~ 310 meV red-shifts (Fig. 4a).

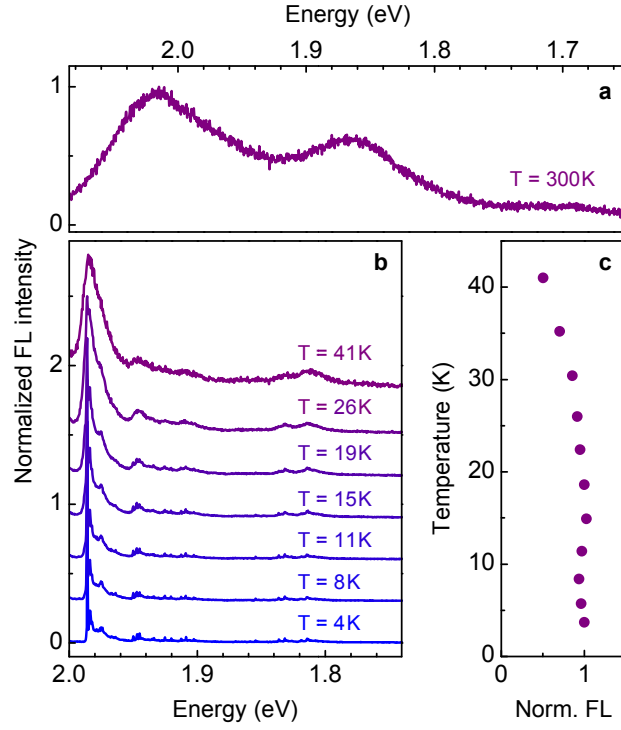


FIG. 4: **a**, Normalized fluorescence spectra of a contaminant in anisole-based PMMA measured at 300 K (reproduced from Fig. 1f of the main text) and **b**, of a similar fluorescence hotspot for selected temperatures ranging from 4 K to 41 K (the traces were offset for clarity). **c**, Total fluorescence normalized to the maximum value at 4 K as a function of temperature. All data were measured with excitation at 532 nm.

Quantum yield estimate

The FL quantum yield of an emitter is given by the ratio of emitted photons to absorbed photons per unit time. In our experiments we estimate the quantum yield of single type 1 fluorescent hotspots in PMMA films formed with anisole-based solutions by scaling the FL intensity to a photostable emitter with known optical properties. We used single nitrogen-vacancy (NV) color centers in bulk diamond that exhibit a quantum yield of $\Phi_{\text{NV}} \simeq 70\%$ [1] and a dipole averaged

absorption cross-section of $\sigma_{\text{NV}} \simeq 3.1 \cdot 10^{-17} \text{ cm}^2$ [2] for 532 nm excitation. With these quantities, the conversion cross-section of a fluorescent hotspot, given by the product of the corresponding quantum yield Φ_{FH} and absorption cross-section σ_{FH} , is determined as:

$$\Phi_{\text{FH}} \sigma_{\text{FH}} = \frac{I_{\text{FH}}}{I_{\text{NV}}} \cdot \frac{\tau_{\text{FH}}}{\tau_{\text{NV}}} \cdot \frac{\Omega_{\text{NV}}}{\Omega_{\text{FH}}} \cdot \Phi_{\text{NV}} \sigma_{\text{NV}}.$$

Here, the term $I_{\text{FH}}/I_{\text{NV}}$ is the FL intensity of a hotspot scaled to the FL of a single NV center for the same excitation power in the linear response regime of both emitters. This ratio ranged from 1.9 to 2.4 for room temperature measurements and peaked at ~ 13.2 for cryogenic temperatures of 3.1 K and 4.2 K. The emitters were excited with continuous wave excitation at 532 nm and circular polarization to ensure averaging over the possible orientations of the transition dipole moments. The factor $\tau_{\text{FH}}/\tau_{\text{NV}}$ accounts for the different FL lifetimes of the fluorescent hotspots and the NV centers with $\tau_{\text{FH}} \simeq 3.6 \text{ ns}$ and $\tau_{\text{NV}} \simeq 12.9 \text{ ns}$ determined experimentally. Finally, we also account for the difference in the effective collection solid angles for fluorescent dipoles embedded in different dielectric environments (PMMA and diamond) with respective refractive indices via $\Omega_{\text{NV}}/\Omega_{\text{FH}}$ which was close to $\simeq 0.35$ in our experiments.

With these values the conversion cross-section of a typical type 1 fluorescent hotspot excited at 532 nm was in the order of $\sim 5 \cdot 10^{-18} \text{ cm}^2$ at room temperature and increased to $\sim 3 \cdot 10^{-17} \text{ cm}^2$ at cryogenic temperatures. Using $\sigma_{\text{FH}} \simeq 1 \cdot 10^{-16} \text{ cm}^2$ as a typical absorption cross-section of the second absorption band of common polycyclic hydrocarbon compounds [3], we obtain an estimate for the fluorescence quantum yield Φ_{FH} of $\sim 5\%$ at room temperature and up to 30% at cryogenic temperatures. We obtained similar values, both at room and cryogenic temperatures, from scaling the quantum yield of fluorescent hotspots in anisole-based samples to fluorescence characteristics of individual TDI molecules.

-
- [1] F. Jelezko and J. Wrachtrup, *Phys. Status Solidi A* **203**, 3207 (2006).
[2] T.-L. Wee, Y.-K. Tzeng, C.-C. Han, H.-C. Chang, W. Fann, J.-H. Hsu, K.-M. Chen, and Y.-C. Yu, *J. Phys. Chem. A* **111**, 9379 (2007).
[3] I. B. Berlman, *Handbook of Fluorescence Spectra of Aromatic Molecules* (Academic Press, 1971), 2nd ed.